

Hydrothermal Growth and Characterization of Nanostructured Vanadium-Based Oxides

Ning Ding,^{†,‡} Shuhua Liu,[‡] Xuyong Feng,[†] Haitao Gao,[§] Xin Fang,[†] Jing Xu,[†]
Wolfgang Tremel,[§] Ingo Lieberwirth,^{*,‡} and Chunhua Chen^{*,†}

Department of Materials Science and Engineering, University of Science and Technology of China,
Hefei 230026, P. R. China, and Max Planck Institute for Polymer Research, Mainz 55128, Germany,
and Institute of Inorganic and Analytical Chemistry, University of Mainz, Mainz 55099, Germany

Received June 18, 2008; Revised Manuscript Received December 22, 2008

ABSTRACT: V_2O_5 nanofibers and three vanadium-based oxides with different structures (MnV_2O_6 nanosheets, $FeVO_4 \cdot 0.92H_2O$ nanoneedles, and $Sn_2VO_6 \cdot 0.78H_2O$ nanoparticles) were synthesized via a hydrothermal method. Field-emission scanning electron microscopy, transmission electron microscopy, electron diffraction, energy dispersive X-ray, and electron energy loss spectroscopy were employed to characterize their morphologies and crystal structures. Electrochemical tests in rechargeable lithium batteries show that among these vanadium-based oxides $Sn_2VO_6 \cdot 0.78H_2O$ nanoparticles exhibit the highest capacity, more than 1700 mAh g^{-1} , and can keep good capacity retention. The magnetic properties of MnV_2O_6 nanosheets and $FeVO_4 \cdot 0.92H_2O$ nanoneedles were also investigated.

1. Introduction

In recent years, the development of portable electronic devices, such as laptops and mobile phones, has led to an explosive demand for high energy density and long life batteries. Compared with other batteries (Pb-acid, Ni-Cd, and Ni-MH), lithium-ion batteries are superior in high capacity, long life, and nonmemory effects, and have the capability to compete with the ever-growing market demand.¹ Vanadium oxides and vanadium-based oxides, such as V_2O_5 , LiV_3O_8 , $Ag_2V_4O_{11}$ and so on, are good host materials for the reversible intercalation and extraction of lithium, and therefore have been widely studied as the electrode materials for lithium-ion batteries.² In addition, the wide range of oxidation states of vanadium from +2 to +5 allows vanadium to potentially transfer more than one electron in application; hence, these materials have the potential to provide higher capacities than the common one-electron-transfer cathode materials, such as $LiCoO_2$, $LiMn_2O_4$, and $LiFePO_4$.³ Actually, $Ag_2V_4O_{11}/Li$ primary batteries have been used in the implantable cardioverter defibrillator to deliver shocks to save the life of cardiopathy patients.⁴ In recent years, several copper vanadium oxides have been also reported as high capacity cathode materials.⁵

Nanostructured materials, such as nanosheets, nanofibers, nanoneedles, and nanoparticles, have attracted much attention due to their superiorities in both physical and chemical properties, and potential applications in catalyst, electronics, and magnetic memory devices.⁶ For example, nanostructured electrode materials usually exhibit a significant superiority in capacity and power rate. Chan et al.⁷ have reported that V_2O_5 nanoribbon shows an ultrafast Li diffusion and probably can be used at a super high power rate (360C). Thus, it is interesting to explore new nanostructured vanadium-based oxides for lithium-ion battery application. Much effort has been devoted to developing new approaches to synthesize the morphology and size controllable nanostructured materials.⁸ Xu et al.⁹

successfully synthesized VO_x nanotubes via a sol–gel method, and Takahashi et al.¹⁰ obtained V_2O_5 nanorod arrays by sol electrophoretic deposition. In addition, other methods, such as thermal deposition and hydrothermal methods, have also been widely used in the synthesis of nanostructured vanadium-based oxides.¹¹

In our previous study, we have synthesized the aligned MnV_2O_5 nanorods.¹² In the present work, a series of nanostructured vanadium-based oxides (MnV_2O_6 nanosheets, $FeVO_4 \cdot 0.92H_2O$ nanoneedles, $Sn_2VO_6 \cdot 0.78H_2O$ nanoparticles and V_2O_5 nanofibers) were synthesized via a hydrothermal method. Their morphologies and structures were extensively studied by transmission electron microscope (morphology, composition, electronic structure and finally crystal structure). Their electrochemical and magnetic properties were also investigated.

2. Experimental Section

Materials. All reagents in the experiments are commercially available from Aldrich, and used without further purification. Ammonium metavanadate (NH_4VO_3), manganese acetate ($Mn(CH_3COOH)_2 \cdot 4H_2O$), ferrous chloride ($FeCl_2 \cdot 4H_2O$), cobaltous chloride ($CoCl_2 \cdot 6H_2O$), nickelous chloride ($NiCl_2$) and stannous chloride ($SnCl_2$).

Preparation of V_2O_5 Fibers and Me-Incorporated (Me = Mn, Fe, Co, Ni, Sn) VO_x . In a typical procedure, 0.2925 g (ca. 2.5 mmol) of NH_4VO_3 , and 0.6129 g (ca. 2.5 mmol, the mol ratio of Me and V was kept to 1:1) of $Mn(CH_3COOH)_2 \cdot 4H_2O$ were added into a 15 mL Teflon-lined stainless-steel autoclave. Then the autoclave was filled with 10 mL of deionized water and 3 mL of 2 M HNO_3 . The autoclave was sealed and kept at 140 °C for 24 h. To obtain homogeneous products, the whole hydrothermal process was carried out under a magnetic stirring. The products were filtrated and washed by deionized water 3 times, and then dried in a vacuum-drybox at 50 °C without further calcinations before the tests.

Characterization. The morphologies of products were characterized by field-emission scanning electron microscopy (FE-SEM, LEO 1530 Gemini). Electron energy loss (EEL) spectra and element mappings images were recorded from a Zeiss 912 microscope operated at 120 kV with an in-column Omega energy filter. Energy loss was calibrated before measurement using a standard NiO_x sample to the peak of $Ni-L_3$ edge at 854 eV. All spectra were recorded using a parallel-mode with a spectral magnification of 163 \times . The energy resolution was about 1.8 eV with an energy dispersion of 0.12 eV pixel⁻¹. Transmission electron microscope (TEM) images and selected area electron diffraction (SAED) were performed on a TECNAI F20 transmission electron

* Corresponding authors. Fax: 49-6131-379 100; e-mail: lieberw@mpip-mainz.mpg.de (I.L.); Fax: 86-551-360-1592; e-mail: cchchen@ustc.edu.cn (C.C.).

[†] University of Science and Technology of China.

[‡] Max Planck Institute for Polymer Research.

[§] University of Mainz.

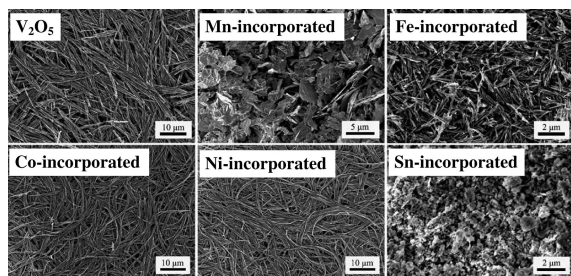


Figure 1. EM images of fiber-like V_2O_5 and other Me (Me = Mn, Fe, Co, Ni, Sn)-incorporated VO_x samples. “Me-incorporated” is used to differentiate them for convenience, although the “Co-incorporated” and “Ni-incorporated” samples are actually V_2O_5 .

microscope with an acceleration voltage of 200 kV. The amount of water in vanadium-based oxides was determined by thermogravimetric analysis (TGA, Shimadzu TA-50). Electrochemical tests were conducted in coin cells (CR2032 size). The working electrode consisted of active powders, carbon black (CB), and polyvinylene difluoride (PVDF) in a weight ratio of 4:3:3. Coin cells were assembled in an argon-filled glovebox (MBraun Labmaster 130) with Li metal as counter electrodes and 1 mol L^{-1} LiPF_6 /ethylene carbonate-diethyl carbonate (EC-DEC, w/w = 1:1) as the electrolyte, and a porous polypropylene membrane (Celgard 2400) as the separator. Galvanostatic charge–discharge tests were carried on a multichannel battery test system (NEWARE BTS-610). Magnetic susceptibilities were measured with a Quantum Design MPMS2 SQUID magnetometer equipped with a 5.5 T magnet operating at 1 T.

3. Results and Discussion

3.1. Morphology and Composition Studies. FE-SEM images are shown in Figure 1. V_2O_5 synthesized via a hydrothermal method exhibits a fiber-like morphology, about 100 nm wide and 10 μm long. Compared with V_2O_5 nanofibers, Mn and Fe-incorporated VO_x (for at this moment the valence of V in vanadium-based oxides is still unknown, VO_x is used instead of V_2O_5) exhibit sheet-like and needle-like morphologies, respectively. For those Co and Ni-incorporated VO_x , similar to that of pure V_2O_5 , both of them are comprised of fiber-like crystallites, whereas these crystallites are banded fibers, instead of rigid fibers like pure V_2O_5 . The morphology of Sn-incorporated VO_x completely changes into nanoparticles.

From the morphologies above, it is clear that after adding the second metallic ions, especially Mn, Fe, and Sn ions, the particle morphologies of V_2O_5 nanofibers have been changed. Now the questions are whether the added metal ions are homogeneously distributed in VO_x lattices and what the compositions of these vanadium-based oxides are. The results of elemental mappings based on EELS of Mn and Fe-incorporated VO_x are shown in Figure 2a–f. The homogeneous color distribution indicates that the Mn and Fe ions have been well-dispersed in VO_x lattices. The TEM and high-resolution TEM images of Sn-incorporated VO_x show that the diameter of Sn-incorporated VO_x nanoparticles is about 5 nm (Figure 2g,h). To determine the final composition, energy dispersive X-ray (EDX) analysis was carried out on Tecnai F20. The EDX results of three vanadium-based oxides are shown in Figure 2i. The EDX spectrum of Mn-incorporated VO_x shows two manganese peaks ($K_\alpha \sim 5.9$ keV, $K_\beta \sim 6.5$ keV) and two vanadium peaks ($K_\alpha \sim 4.9$ keV, $K_\beta \sim 5.4$ keV). The emission peaks of iron are at ~ 6.4 keV (K_α) and 7.0 keV (K_β). Because of the more complicated electron shell structure, Sn L lines exhibit a series of emission peaks from 3.2 to 4.5 keV. The quantified analyses of the EDX spectra show that metallic elements ratios (Me:V) are 1:2 for Mn-incorporated, 1:1 for Fe-incorporated, and 2:1

for Sn-incorporated vanadium oxides. Because of the resolution restriction of our TEM machine (Zeiss 912) equipped with energy-filter for the EEL spectra, the element mappings of Sn-incorporated VO_x are absent. On the other hand, the EDX analysis shows that the distribution of Sn in Sn-incorporated VO_x is also homogeneous. It should be mentioned that almost no signals of Co and Ni are detected in Co and Ni-incorporated vanadium oxides (results not shown here), indicating that Co and Ni ions are not incorporated into VO_x lattices. Nevertheless, the additions of Co and Ni ions in the hydrothermal process seem to increase the interior stress in VO_x lattices during its growth so that banded VO_x fibers are formed. It has been reported that the V_2O_5 fibers can provide high Young’s modulus and high actuator-generated stress.¹³ Therefore, the artificially banded VO_x fibers might be interesting for the actuators application in the conversion of chemical energy to mechanical energy.

3.2. Valence and Structure Studies. The valences of incorporated metallic and vanadium ions are determined by the EEL spectra of Mn, Fe, and Sn-incorporated VO_x (Figure 3). The EEL spectra of Mn L-edge from Mn-incorporated VO_x exhibit two distinct white lines with maximum peaks at 641.6 (L_3 , corresponding to four $2p^{3/2} \rightarrow 3d^{3/2} 3d^{5/2}$) and 653.2 eV (L_2 , corresponding to two $2p^{1/2} \rightarrow 3d^{3/2}$), respectively (Figure 3a).¹⁴ By comparing the absolute energy position of the white-lines and their intensity ratio (L_3/L_2), it can be determined that the valence of Mn in Mn-incorporated VO_x is +2 and the valence of Fe in Fe-incorporated VO_x is +3 (Figure 3a,b). The valence increase of Fe indicates that Fe^{2+} in the precursor is oxidized during the hydrothermal process. The EEL spectra of V L-edge also show two peaks at 519.8 and 526.4 eV, and the following peaks at the high energy loss correspond to the O K-edge (Figure 3c).¹⁵ Hence, the valences of V in Mn and Fe-incorporated samples are still +5, which indicates that the oxidation of Fe^{2+} is either due to the oxygen dissolved in water or due to the nitric acid added to dissolve ammonium metavanadate. In combination with the EDX results, it is clear now that the composition of Mn-incorporated VO_x is $\text{MnV}_2\text{O}_6 \cdot x\text{H}_2\text{O}$ and the composition of Fe-incorporated VO_x is $\text{FeVO}_4 \cdot x\text{H}_2\text{O}$. The water content (x) will be determined later by TGA. For the supposedly Co and Ni-incorporated samples, no real incorporation of Co and Ni-ions into the VO_x lattice is detected by EDX spectra (not shown), and the valence of V still remains at +5, which is confirmed by EEL spectra (not shown). Thus, the banded fibers are still V_2O_5 . For Sn-incorporated sample, its EEL spectra show that the valence of V decreases from +5 to +4, indicating a possible oxidation of Sn^{2+} in the precursor (Figure 3d). Because of the highly overlapping of Sn M-edge and O K-edge (the energy loss from 530 to 550 eV), it is difficult to determine the final oxidation state of Sn ions. As we also cannot find any possible composition of Sn-incorporated vanadium oxides on the JCPDS cards, we assume that the composition of Sn-incorporated VO_x is $\text{Sn}_2\text{V(IV)O}_6 \cdot x\text{H}_2\text{O}$ at this moment.

The TEM images and SAED patterns of the incorporated samples are shown in Figure 4. The SAED pattern of $\text{MnV}_2\text{O}_6 \cdot x\text{H}_2\text{O}$ is shown in the inset of Figure 4a. By indexing the diffraction pattern, the distances of (200) and ($\bar{1}10$) planes fit those of MnV_2O_6 (space group: $C2/m$, JCPDS 35-0139). In other words, the water content (x) in $\text{MnV}_2\text{O}_6 \cdot x\text{H}_2\text{O}$ is 0. On the other hand, for $\text{FeVO}_4 \cdot x\text{H}_2\text{O}$, the sample is not stable under the high electron energy density (the inset in Figure 4b), indicating that there is some water in its crystal lattice. According to the TGA curves of $\text{FeVO}_4 \cdot x\text{H}_2\text{O}$ and

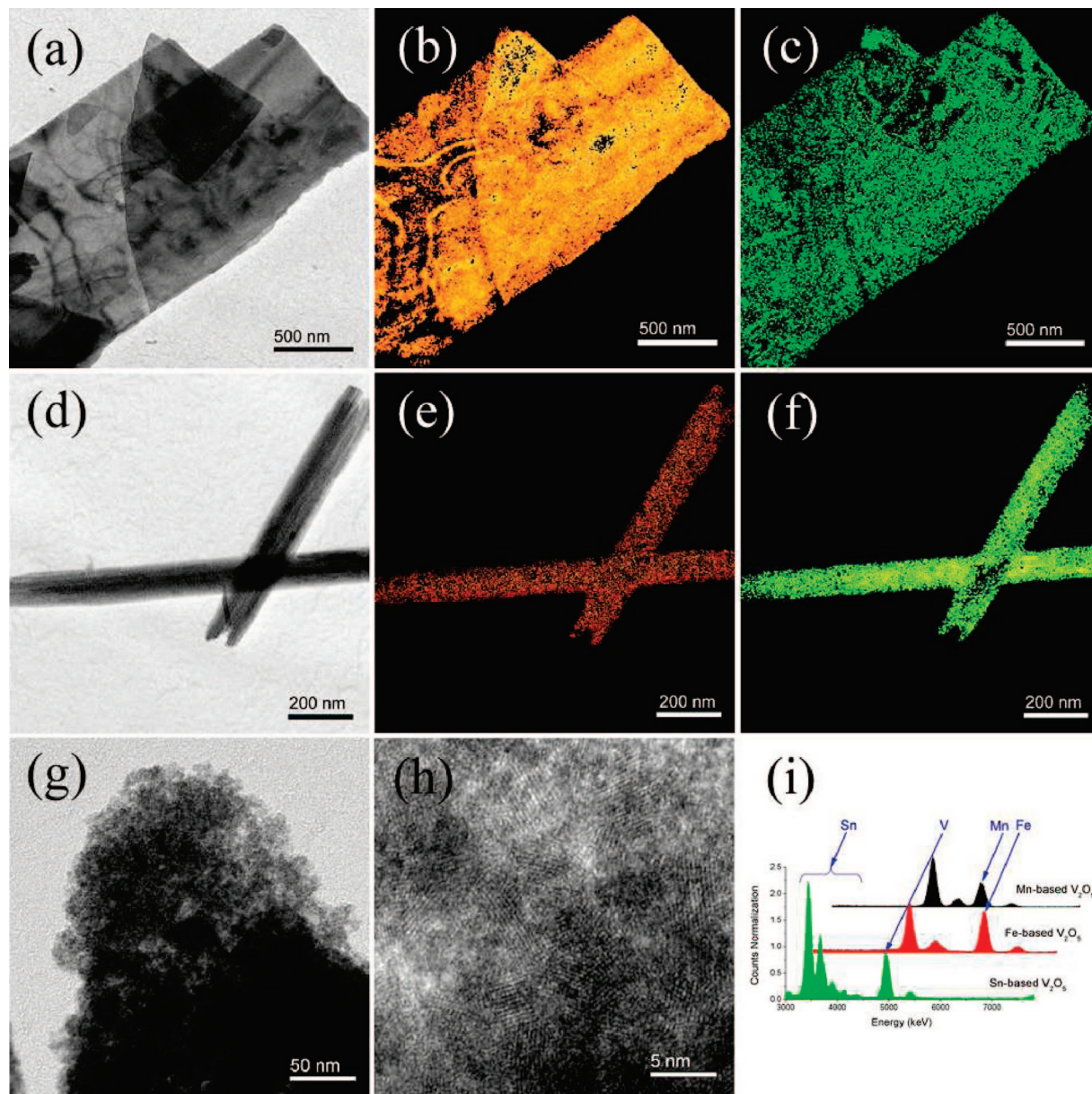


Figure 2. (a) Bright-field TEM image of sheet-like Mn-incorporated VO_x, and its element mapping images for Mn (b) and V (c). (d) Bright-field TEM image of needle-like Fe-incorporated VO_x, and its element mapping images for Fe (e) and V (f). (g, h) TEM and high-resolution TEM images of Sn-incorporated VO_x nanoparticles. (i) EDX spectra of Mn-incorporated VO_x, Fe-incorporated VO_x, and Sn-incorporated VO_x.

Sn₂V(IV)O₆·*x*H₂O (not shown here), the compositions are FeVO₄·0.92H₂O and Sn₂VO₆·0.78H₂O. In addition, by measuring the distance of diffraction rings of Sn₂VO₆·0.78H₂O (the inset in Figure 4c), it almost fits that of SnO₂ (space group: *P4₂/mmn*). For SnO₂, its *d*₍₁₁₀₎ is 3.36 Å, *d*₍₁₀₁₎ is 2.65 Å, and *d*₍₂₁₁₎ is 1.77 Å. According to the diffraction pattern of Sn₂VO₆·0.78H₂O, its *d*₍₁₁₀₎ is 3.4 Å, *d*₍₁₀₁₎ is 2.7 Å and *d*₍₂₁₁₎ is 1.8 Å. The differences in *d* values between SnO₂ and Sn₂VO₆·0.78H₂O are very small, which means that Sn₂VO₆ may be rewritten as Sn_{4/3}V_{2/3}O₄, that is, 2/3 of Sn(IV) ions in SnO₂ are substituted by V(IV) without destroying its original crystalline structure.

3.3. Electrochemical Properties in Rechargeable Lithium Batteries. One application field of these vanadium-based oxides is in lithium-ion batteries. For example, MnV₂O₆ has a structure consisting of chains of edge-sharing MnO₆ disordered octahedra connected by chains of corner and edge-sharing VO₆ octahedra along the *b* axis. This structure provides a large amount of rather open spaces between MnO₆ and VO₆ octahedra, which are

suitable for lithium intercalation and extraction.¹⁶ Thus, these vanadium-based oxides are the candidate electrode materials for lithium-ion batteries.¹⁷ Galvanostatic charge–discharge profiles of fiber-like V₂O₅, sheet-like MnV₂O₆, needle-like FeVO₄·0.92H₂O and Sn₂V(IV)O₆ nanoparticles are shown in Figure 5. At the beginning of discharge, V₂O₅ and FeVO₄·0.92H₂O exhibit short plateaus from 3 to 2 V, with a capacity of 160 mAh g^{−1} and 176 mAh g^{−1}, respectively, which correspond to forming solid solutions of Li_{1.1}V₂O₅ and Li_{1.3}FeVO₄·0.92H₂O (Figure 5a,b). For the voltage profile of FeVO₄·0.92H₂O, there is another plateau at around 1.65 V, whereas it does not exist in the voltage profile of FeVO₄.¹⁸ Thus, we propose that the plateau at 1.65 V results from the crystalline water (Figure 5c). Furthermore, in our recent study, we have also found a similar plateau at 1.73 V when the electrolyte contains a carboxyl species, which is consistent with the theoretical thermo-dynamics calculation result.¹⁹ For Sn₂VO₆·0.78H₂O, there is also a short plateau at 1.4 V

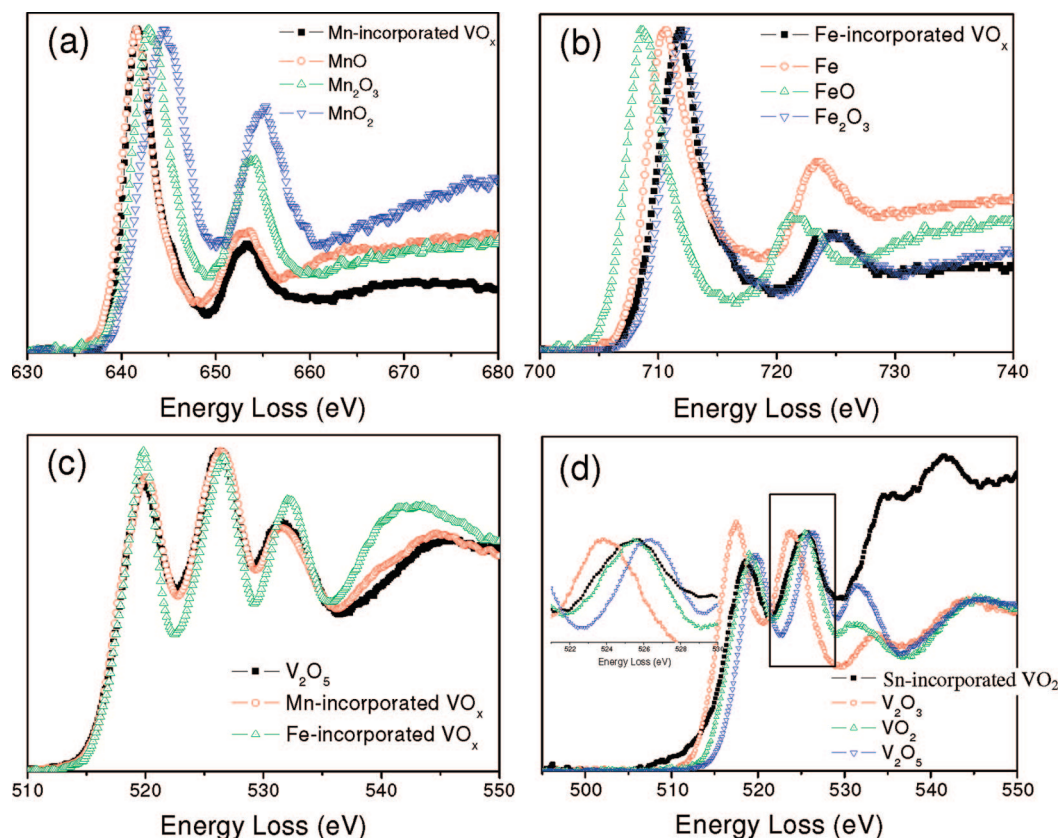


Figure 3. EEL spectra of (a) Mn L-edge from Mn-incorporated VO_x , (b) Fe L-edge from Fe-incorporated VO_x , and (c) V L-edge from fiber-like V_2O_5 , Mn-incorporated VO_x and Fe-incorporated VO_x . (d) EEL spectra of Sn M-edge and O K-edge from Sn-incorporated VO_x .

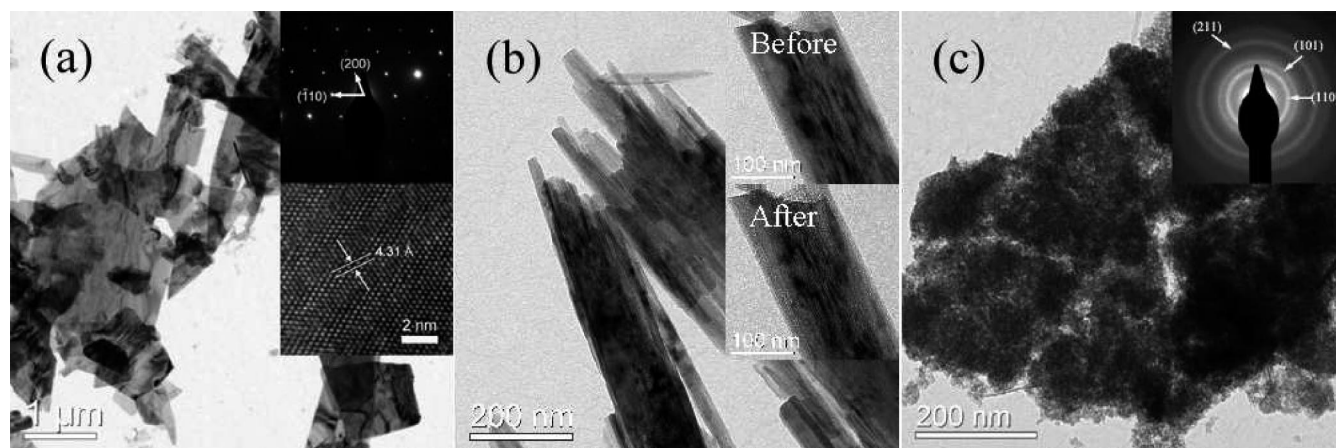


Figure 4. TEM images and SAED patterns of (a) MnV_2O_6 nanosheets, (b) $\text{FeVO}_4 \cdot 0.92\text{H}_2\text{O}$ nanoneedles, and (c) $\text{Sn}_2\text{VO}_6 \cdot 0.78\text{H}_2\text{O}$ nanoparticles.

corresponding to the reaction between crystalline water and lithium (Figure 5d). According to the capacity resulting from the crystalline water, we can also roughly calculate the amount of water in $\text{FeVO}_4 \cdot 0.92\text{H}_2\text{O}$ and $\text{Sn}_2\text{VO}_6 \cdot 0.78\text{H}_2\text{O}$, which agrees well with the results concluded from the TGA curves. For all samples, they show long plateaus when the voltage drops to 1 V, which correspond to a complex reduction process. Piffard et al.²⁰ have reported that after being full discharged, MnV_2O_7 (another manganese vanadium oxide, where the valence of Mn is +4) can insert large amounts of Li and is with a final composition of $\text{Li}_{12}\text{MnV}_2\text{O}_7$, whereas X-ray absorption spectra and EEL spectra indicate that the oxidation state of Mn^{4+} changes to +2 and V^{5+} cations are only reduced to V^{3+} .

Obviously, the charge is not balanced in $\text{Li}_{12}\text{Mn(II)V}_2\text{(III)O}_7$. The authors proposed that only 50% of electron in Li can transfer to the host matrix, and recently, we have also proposed another mechanism, interfacial lithium storage mechanism, to explain this phenomenon.²¹ Though the discharge capacity of V_2O_5 fibers and MnV_2O_6 nanosheets can reach about 800 mAh g^{-1} , more than twice as that of graphite, which has been widely used in commercial batteries, their cycling capacities are low and fade fast (Figure 5a,b). The low cycling capacity and poor cycling performance are probably associated with their structure failure during lithium intercalation. Both $\text{FeVO}_4 \cdot 0.92\text{H}_2\text{O}$ and $\text{Sn}_2\text{VO}_6 \cdot 0.78\text{H}_2\text{O}$ exhibit higher capacities (more than 1650 mAh g^{-1}) and better cycling performances than V_2O_5 and

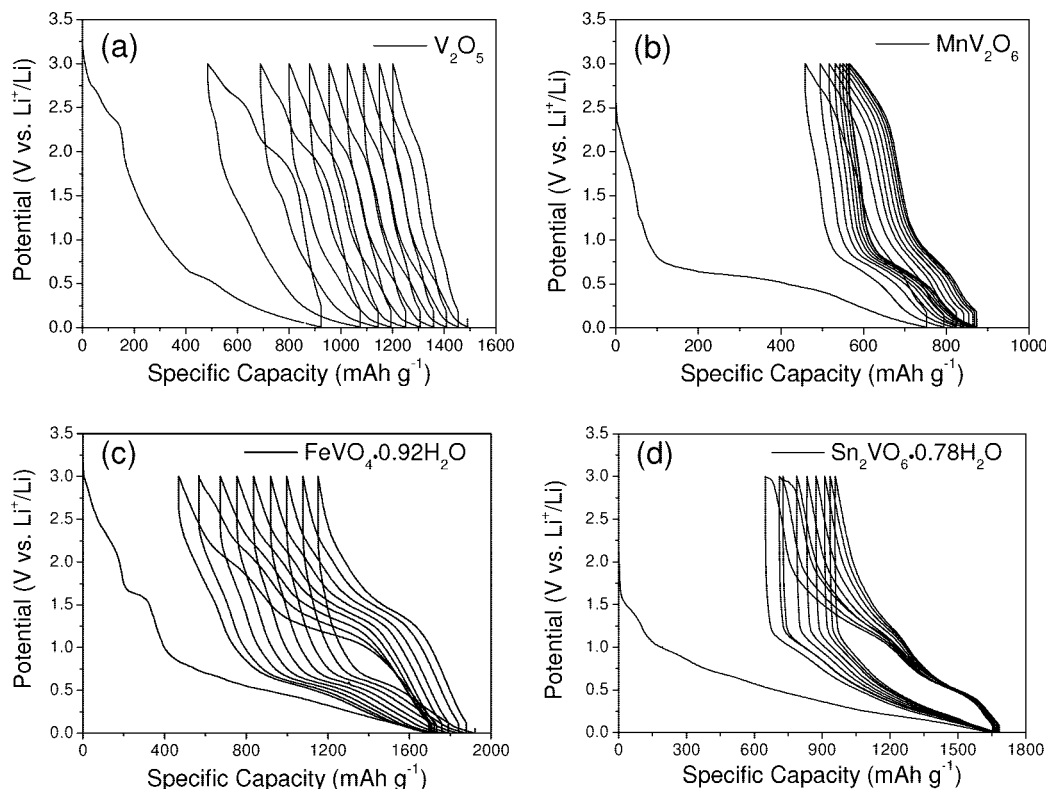


Figure 5. Galvanostatic charge-discharge profiles of (a) V_2O_5 , (b) MnV_2O_6 , (c) $\text{FeVO}_4 \cdot 0.92\text{H}_2\text{O}$, and (d) $\text{Sn}_2\text{VO}_6 \cdot 0.78\text{H}_2\text{O}$ as working materials for rechargeable lithium batteries.

MnV_2O_6 . In addition, for $\text{FeVO}_4 \cdot 0.92\text{H}_2\text{O}$, due to the existence of more crystalline water, which can react with lithium and damage the structure, its cycling performance is not as good as that of $\text{Sn}_2\text{VO}_6 \cdot 0.78\text{H}_2\text{O}$ (Figure 5c,d). Among these four vanadium-based oxides, $\text{Sn}_2\text{VO}_6 \cdot 0.78\text{H}_2\text{O}$ shows the best electrochemical properties and might be further used as anode material in commercial lithium-ion batteries.

3.4. Magnetic Properties. Because of the incorporation of Mn(II) and Fe(III) respectively into the lattices of V_2O_5 , it is interesting to study their magnetic properties. The superconducting quantum interference device (SQUID) measurement shows that the Neel temperatures for MnV_2O_6 and $\text{FeVO}_4 \cdot 0.92\text{H}_2\text{O}$ are 18.4 and 18.5 K, respectively (Figure 6). According to the Curie-Weiss Law $\chi = C/(T - \theta)$, where χ is the magnetic susceptibility, C is a material-specific Curie constant, and θ is the Weiss temperature, we may deduce from the linear fit that $\theta = -0.3$ K, $\mu_{\text{eff}} = 5.80 \mu_{\text{B}}$ for MnV_2O_6 and $\theta = -86.4$ K, $\mu_{\text{eff}} = 5.80 \mu_{\text{B}}$ for $\text{FeVO}_4 \cdot 0.92\text{H}_2\text{O}$, where $\mu_{\text{eff}} = (8C)^{1/2}$. The effective moment $5.80 \mu_{\text{B}}$ for MnV_2O_6 is close to what Kimber et al.²² reported and the expected value $5.92 \mu_{\text{B}}$. As for $\text{FeVO}_4 \cdot 0.92\text{H}_2\text{O}$, the negative Weiss temperature implies the antiferromagnetic interaction nature of this material.

4. Conclusion

In summary, V_2O_5 nanofibers and other three vanadium-based oxides (MnV_2O_6 nanosheets, $\text{FeVO}_4 \cdot 0.92\text{H}_2\text{O}$ nanoneedles and $\text{Sn}_2\text{VO}_6 \cdot 0.78\text{H}_2\text{O}$ nanoparticles) have been successfully synthesized via a simple hydrothermal route at low temperature (140 °C) using NH_4VO_3 as the precursor. Their structures are determined by a series of techniques in TEM, such as EDX, EELS, and ED patterns. Results show that Mn, Fe, and Sn ions are well incorporated into VO_x lattices. In addition, although other two ions (Co^{2+} and Ni^{2+}) cannot be incorporated into VO_x

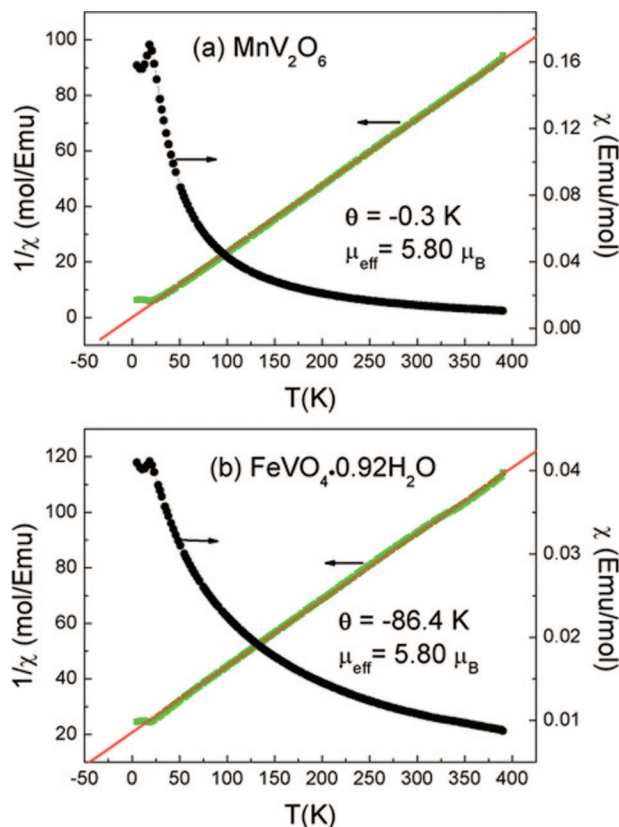


Figure 6. Magnetic properties of (a) MnV_2O_6 and (b) $\text{FeVO}_4 \cdot 0.92\text{H}_2\text{O}$.

lattices, their presence in the hydrothermal process seems to increase the interior stress in VO_x lattices during the crystal

growth and results in bended V_2O_5 fibers, which might be interesting for the actuators application in the conversion of electrical energy to mechanical energy. The electrochemical properties of V_2O_5 nanofibers, MnV_2O_6 nanosheets, $FeVO_4 \cdot 0.92H_2O$ nanoneedles, and $Sn_2VO_6 \cdot 0.78H_2O$ nanoparticles have been investigated in rechargeable lithium batteries. Electrochemical performances show that $Sn_2VO_6 \cdot 0.78H_2O$ nanoparticles exhibit the highest capacity and good capacity retention. The SQUID data show that the Neel temperatures for MnV_2O_6 and $FeVO_4 \cdot 0.92H_2O$ are 18.4 and 18.5 K, respectively. We anticipate our studies can explore a new electrode material, such as $Sn_2VO_6 \cdot 0.78H_2O$ nanoparticles, for further application in commercial lithium-ion batteries.

Acknowledgment. N.D. thanks the financial support of the doctoral promotion program launched between Chinese Academy of Sciences and Max-Planck-Gesellschaft.

References

- (1) Tarascon, J.-M.; Armand, M. *Nature* **2001**, *414*, 359.
- (2) (a) Cao, A.-M.; Hu, J.-S.; Liang, H.-P.; Wan, L.-J. *Angew. Chem., Int. Ed.* **2006**, *44*, 4391. (b) Kannan, A. M.; Manthiram, A. *J. Power Sources* **2006**, *159*, 1405. (c) Garciaalvarado, F.; Tarascon, J.-M. *Solid State Ionics* **1994**, *73*, 247.
- (3) (a) Mizushima, K.; Jones, P. C.; Wiseman, P. J.; Goodenough, J. B. *Mater. Res. Bull.* **1980**, *15*, 783. (b) Tarascon, J.-M.; Wang, E.; Shokoohi, F. K.; McKinnon, W. R.; Colson, S. *J. Electrochem. Soc.* **1991**, *138*, 2859. (c) Padhi, A. K.; Nanjundaswamy, K. S.; Goodenough, J. B. *J. Electrochem. Soc.* **1997**, *144*, 1188.
- (4) (a) Crespi, A. M.; Skarstad, P. M. U. S. Patent 5,458,997. (b) Beninati, S.; Fantuzzi, M.; Mastragostino, M.; Soavi, F. *J. Power Sources* **2006**, *157*, 483.
- (5) (a) Morcrette, M.; Rozier, P.; Dupont, L.; Mugnier, E.; Sannier, L.; Galy, J.; Tarascon, J.-M. *Nat. Mater.* **2003**, *2*, 755. (b) Ma, H.; Zhang, S. Y.; Ji, W. Q.; Tao, Z. L.; Chen, J. *J. Am. Chem. Soc.* **2008**, *130*, 5361.
- (6) (a) Wu, Y.; Xiang, J.; Yang, C.; Lu, W.; Lieber, C. M. *Nature* **2004**, *430*, 61. (b) Hu, Y.-S.; Guo, Y.-G.; Sigle, W.; Hore, S.; Balaya, P.; Maier, J. *Nat. Mater.* **2006**, *5*, 713. (c) Lee, H.; Cho, J. *Nano Lett.* **2007**, *7*, 2638. (d) Sun, Y.; Salamon, M. B.; Garnier, K.; Averbach, R. S. *Phys. Rev. Lett.* **2003**, *91*, 167206.
- (7) Chan, C. K.; Peng, H. L.; Twisten, R. D.; Jarausch, K.; Zhang, X. F.; Cui, Y. *Nano. Lett.* **2007**, *7*, 490.
- (8) (a) Liu, B.; Zeng, H. C. *J. Am. Chem. Soc.* **2003**, *125*, 4430. (b) Cushing, B. L.; Kolesnichenko, V. L.; O'Connor, C. J. *Chem. Rev.* **2004**, *104*, 3893. (c) Lakshmi, B. B.; Dorhout, P. K.; Martin, C. R. *Chem. Mater.* **1997**, *9*, 857. (d) Wu, Y. Y.; Fan, R.; Yang, P. D. *Nano Lett.* **2002**, *2*, 83.
- (9) Xu, J. F.; Czerw, R.; Webster, S.; Carroll, D. L.; Ballato, J.; Nesper, R. *Appl. Phys. Lett.* **2002**, *81*, 1711.
- (10) Takahashi, K.; Wang, Y.; Cao, G. Z. *Appl. Phys. Lett.* **2005**, *86*, 053102.
- (11) (a) Mao, C. J.; Wu, X. C.; Pan, H. C.; Zhu, J. J.; Chen, H. Y. *Nanotechnology* **2005**, *16*, 2892. (b) Liu, Y.; Qian, Y. T. *J. Inorg. Mater.* **2007**, *22*, 1139. (c) Ban, C. M.; Whittingham, M. S. *Solid State Ionics* **2008**, *179*, 1721. (d) Díaz-Guerra, C.; Piqueras, J. *Cryst. Growth Des.* **2008**, *8*, 1031.
- (12) Lei, S. J.; Tang, K. B.; Jin, Y.; Chen, C. H. *Nanotechnology* **2007**, *18*, 175605.
- (13) (a) Gu, G.; Schmid, M.; Chiu, P.-W.; Minett, A.; Frayssé, J.; Kim, G.-T.; Roth, S.; Kozlov, M.; Muñoz, E.; Baughman, R. H. *Nat. Mater.* **2003**, *2*, 316. (b) Biette, L.; Carn, F.; Maugey, M.; Achard, M.-F.; Maquet, J.; Steunou, N.; Livage, J.; Serier, H.; Backov, R. *Adv. Mater.* **2005**, *17*, 2970.
- (14) Schmid, H. K.; Mader, W. *Micron* **2006**, *37*, 426.
- (15) Mitterbauer, C.; Kothleitner, G.; Grogger, W.; Zandbergen, H.; Freitag, B.; Tiemeijer, P.; Hofer, F. *Ultramicroscopy* **2003**, *96*, 469.
- (16) Kim, S.-S.; Ikuta, H.; Waihiara, M. *Solid State Ionics* **2001**, *139*, 57.
- (17) (a) Leroux, F.; Piffard, Y.; Ouvrard, G.; Mansot, J.-L.; Guyomard, D. *Chem. Mater.* **1999**, *11*, 2948. (b) Hara, D.; Shirakawa, J.; Ikuta, H.; Uchimoto, Y.; Wakihara, M.; Miyayama, T.; Watanabe, I. *J. Mater. Chem.* **2002**, *12*, 3717. (c) Patoux, S.; Richardson, T. J. *Electrochem. Commun.* **2007**, *9*, 485.
- (18) Poizot, P.; Baudrin, E.; Laruelle, S.; Dupont, L.; Touboul, M.; Tarascon, J.-M. *Solid State Ionics* **2000**, *138*, 31.
- (19) Ding, N.; Yao, Y. X.; Zhu, J.; Chen, C. H. *J. Appl. Electrochem.* DOI 10.1007/s10800-008-9747-4.
- (20) Piffard, Y.; Leroux, F.; Guyomard, D.; Mansot, J.-L.; Tournoux, M. *J. Power Sources* **1997**, *68*, 698.
- (21) (a) Chen, C. H.; Ding, N.; Wang, L.; Yu, Y.; Lieberwirth, I. J. *Power Sources* (doi: 10.1016/j.jpowsour.2008.10.052). (c) Jamnik, J.; Maier, J. *Phys. Chem. Chem. Phys.* **2003**, *5*, 5215. (d) Zhukovskii, Y. F.; Balaya, P.; Kotomin, E. A.; Maier, J. *Phys. Rev. Lett.* **2006**, *96*, 058302.
- (22) Kimber, S. A. J.; Attfield, J. P. *Phys. Rev. B* **2007**, *75*, 064406.

CG800645C